




Article

Nickel-Cadmium-Sulfide Anchored on rGO Nanocomposite for Removal of Textile Industry Dyes

Narthana Kandhasamy¹, Govindasamy Murugadoss^{1,*} , Thiruppathi Kannappan², Kamalan Kirubaharan³ 
and Rajesh Kumar Manavalan⁴ 

¹ Centre for Nanoscience and Nanotechnology, Sathyabama Institute of Science and Technology, Chennai 600119, Tamil Nadu, India

² Department of Physics, SRM Valliammai Engineering College, SRM Nagar, Kattankulathur 603203, Tamil Nadu, India

³ Coating Department, Fun Glass-Centre for Functional and Surface Functionalised Glass, Alexander Dubcek University of Trencin, 91150 Trencin, Slovakia

⁴ Institute of Natural Science and Mathematics, Ural Federal University, 620002 Yekaterinburg, Russia

* Correspondence: murugadoss_g@yahoo.com

Abstract: The design and development of a novel route for the preparation of efficient photocatalysts for the treatment of polluted water is an essential need. Due to rapid expansion of pharmaceutical and textile industries, the discharge of drugs and sewage contaminants leads to water contamination. To address these issues, hydrothermally synthesized Ni–Cd–S/rGO nanocomposite with a cauliflower structure was developed. The prepared nanocomposite was studied using advanced characterization techniques to confirm crystal structure, surface morphology, optical studies and material composition in detail. Further, the photodegradation process of textile-based Methylene Blue (MB) and Methyl Orange (MO) dyes using Ni–Cd–S/rGO nanocomposite with desired time interval under natural sunlight was also investigated. The maximum photocatalytic performance of > 90% was achieved for the photocatalyst. The photodegradation rate can be maintained after 5 recycling tests in the presence of MB and MO dyes. The remarkable degradation efficiency, high rate constant and reusability of the Ni–Cd–S/rGO nanocomposite make it an excellent choice for textile effluent treatment.

Keywords: hydrothermal; reduced graphene oxide; nanocomposite; photodegradation; scavenger; methylene blue; methyl orange



check for updates

Citation: Kandhasamy, N.; Murugadoss, G.; Kannappan, T.; Kirubaharan, K.; Kumar Manavalan, R. Nickel-Cadmium-Sulfide Anchored on rGO Nanocomposite for Removal of Textile Industry Dyes. *Sustainability* **2022**, *14*, 16184. <https://doi.org/10.3390/su142316184>

Academic Editor: Haradhan Kolya

Received: 23 October 2022

Accepted: 1 December 2022

Published: 4 December 2022

Publisher's Note: MDPI stays neutral with regard to jurisdictional claims in published maps and institutional affiliations.



Copyright: © 2022 by the authors. Licensee MDPI, Basel, Switzerland. This article is an open access article distributed under the terms and conditions of the Creative Commons Attribution (CC BY) license (<https://creativecommons.org/licenses/by/4.0/>).

1. Introduction

The organic dyes discharged from textile industries into sewage water cause serious consequences for aquatic life and human health. Many methods, including adsorption, coagulation, reverse osmosis and ion adsorption, are used to remove toxic pollutants from wastewater. The above methods are limited due to their high cost, difficulty in handling and removal of primary pollutants that need further treatment [1]. In this regard, the research community paid close attention to the above problems in order to eliminate various types of hazardous organic pollutants from various sources, and photocatalyst was regarded as a promising traditional technology [2]. However, for us to achieve practical application, building an effective and stable photocatalyst system is a significant challenge. Because of their powerful redox (oxidation and reduction) processes under sunlight irradiation, semiconductors based photocatalysts can solve the problem of water pollution efficiently [3,4]. Many new semiconductor materials, such as those based on bismuth-based materials [5], metallic oxide [6], graphitic carbon nitrate materials [7] and barium-based materials [8], are frequently used in photocatalysis. However, the above semiconductors lack the benefits of being inexpensive, highly effective, stable, non-toxic, environmentally friendly and having a small band gap, which can fully utilize solar energy. Therefore, it is very important to investigate photocatalysts that respond to visible light.

Scientists are currently very interested in developing visible light-driven photocatalysts with an appropriate band gap by combining them with multi-component materials, doping with co-catalysts and creating heterojunctions [9].

Due to their reduced electron-hole pair recombination, increased light absorption range, spatially separated active sites and enhanced photocatalytic activity, binary and ternary type semiconductors are currently a focal point in the photocatalytic field [10,11]. The notable semiconductor cadmium sulfide (CdS) has gained renewed interest due to its unique properties, which include a high carrier transport capacity and a narrow band gap that can effectively utilize sunlight ($\lambda < 516$ nm). Moreover, due to their high surface energy, CdS nanoparticles are easily aggregated, resulting in absence of active sites. Therefore, nanoparticles based on CdS are prepared as composites with other ternary sulfide and carbon materials, such as CdS/Graphene [12], CdS/Pt-TiO₂ [13], N-CDs/CdS [14], CdS/NiCd [15] and CdS/NiSe [16] are reported. For example, Katori and his team effectively synthesized pure SnO₂, CdS and combination of CdS/SnO₂ containing (1,3,5,8 and 10 wt% CdS), respectively. The synthesized heterostructure photocatalysis showed high degradation of MB dye under both UV and natural sunlight irradiations. SnCd₅ nanoparticles possess excellent photocatalytic stability of 83 and 94% under UV and natural sunlight radiations, respectively [17]. Hou [18] and Singh [19] reported the synergistic action of CdS on TiO₂ and Ag nanoparticles and the outstanding photocatalytic property was obtained in the degradation of MO dye. Kokilavani et al. [20] synthesized heterostructure nanocomposite of NiS/Ag₂MoO₄, revealing the photocatalytic property of MB as 90.8% photodegradation process. Therefore, the NiS/CdS nanoparticle is effective for the degradation of organic dye released from textile industry. Moreover, NiS/CdS have excellent photocatalytic activity due to their enhanced photoelectron-hole separation efficiency, improved light corrosion resistance of CdS, increased photo-response region of sunlight and accelerated mobility of the photogenerated carriers. Due to their low cost, relatively high electronic conductivity and abundance of surface-active sites, the typical mixed transition-metal sulfide of nickel sulfide (NiS) and CdS is currently used extensively in electrochemistry. The multiple oxidation states of the Ni and Cd redox couple pairs have been demonstrated to provide excellent conductivity [21]. The NiS can facilitate electron transport and contaminant adsorption in water due to its specific surface area and high electronic conductivity. The NiS anchored with CdS nanoparticles and reduced graphene oxide (rGO) may able to inhibit light corrosion, which will greatly improve the composite's stability and photocatalytic capability. The addition of rGO could significantly improve Ni-Cd-S stability and crystallinity in the nanocomposite. To our knowledge, no studies on Ni-Cd-S/rGO nanocomposites with superior photocatalytic performance have been reported [22].

Here, we report a novel Ni-Cd-S/rGO nanocomposite as an effective photocatalyst to remove the dye molecules presented in textile waste water. For the synthesis of NiS, CdS, Ni-Cd-S and Ni-Cd-S/rGO nanocomposite, a one-step hydrothermal process was used at 160 °C for 24 h. The best-performing Ni-Cd-S/rGO showed excellent photocatalytic performance of MB and MO dyes removal percentages of 94 and 97.1% under irradiation of sunlight. In the meantime, the prepared Ni-Cd-S/rGO can exhibit long-term stability and recyclability tests even after five cycles.

2. Materials and Methods

2.1. Materials

Cadmium nitrate tetrahydrate Cd(NO₃)₂, nickel (II) nitrate hexahydrate Ni(NO₃)₂·6H₂O, cetyltrimethylammonium bromide (CTAB), graphite, sodium nitrate (NaNO₃), potassium permanganate (KMnO₄), thiourea (NH₂CSNH₂) and sodium hydroxide (NaOH) were procured from Sigma Aldrich. Concentrated sulfuric acid (H₂SO₄), hydrazine hydrate (N₂H₂·H₂O), hydrogen peroxide (H₂O₂), hydrochloric acid (HCl), ethanol, acetone and deionized (DI) water were purchased from Sisco Research Laboratory (SRL), India. All the chemicals were used for synthesis without further processing.

2.2. Preparation of Ni–Cd–S/rGO

Ni–Cd–S/rGO nanocomposite was prepared through hydrothermal technique. In a typical synthesis, Ni(NO₃)₂·6H₂O (0.5 M) and Cd(NO₃)₂ (0.5 M) were dissolved in 60 mL of DI water under 30 min of stirring. One gram of CTAB and 200 mg of rGO were added to the above solution and stirred for another 30 min. Then, thiourea (0.5 M) was added dropwise slowly in the above solution. After 1 h, the resulting solution was transferred into a hydrothermal reaction at 160 °C for 24h. Finally, a solid black color sample was collected after centrifugation, which was washed three times with acetone and DI water, and then the product was dried overnight at 100 °C. Similarly, a pristine NiS, CdS and Ni–Cd–S were obtained by the same procedure without rGO. The rGO was prepared using a modified Hummers' technique [23].

2.3. Material Characterization

The crystal structure of the prepared composites was determined using X-ray diffraction (XRD) with Cu-K α radiation ($\lambda = 1.5418 \text{ \AA}$) recorded by BRUKER D8 Advance, Davinci in the scanning range of 20 to 80 degrees. A Fourier transform infrared (FTIR) spectrophotometer was employed to record elements in mid IR range on a PerkinElmer-1600 spectrometer. KBr was used as a reference material. On a PHI5000 Version Probe III, elemental information of produced photocatalysts was obtained using X-ray photoelectron spectroscopy (XPS). The microstructures of the nanocomposites were studied using high-resolution scanning electron microscopy (HR-SEM) recorded using a Thermo Scientific ApreoS and high-resolution transmission electron microscopy (HR-TEM) at an acceleration voltage of 200 kV in JEOL Japan's JEM-2100 Plus. A UV-vis spectrophotometer (SYSTRON-ICS, Double beam spectrometer 2203) was used to record the diffuse reflectance spectra of the produced photocatalysts.

2.4. Photocatalytic Degradation of Textile Dye

The photocatalytic degradation of the generated materials in sunlight was investigated using MB and MO dyes. Twenty-five milligrams of the produced sample was mixed with 50 mL of dye solution (20 ppm). Then, the dye solution was kept exposed to direct sunshine for 2.5 h. During the irradiation process, predefined intervals of 2 mL dye solutions were removed from the apparatus. The maximum absorbance for MB and MO is reported to be 662 nm and 464 nm [24]. The maximum absorbance change was used to analyze the degradation of MB and MO using a UV-Vis spectrophotometer. The formula for calculating deterioration efficiency is as follows [24]:

$$\text{Degradation efficiency (\%)} = [(C_0 - C)/C_0] \times 100 \quad (1)$$

where C represents initial concentration and C₀ denotes concentration at in equilibrium condition. The treated catalyst was centrifuged, washed with acetone/H₂O solution, and kept dried at 75 °C after first cycle to carry out the catalytic stability experiment. In addition, the first-order kinetic study was employed to calculate the accurate depolluting rate, as follows [24]:

$$-\ln(C/C_0) = kt \quad (2)$$

where k denotes the rate of reaction constant and t represents the duration. The photocatalytic research was to achieve an average light intensity of 0.85×10^5 lux. A pH impact and catalyst dose investigation were also carried out. The photocatalytic study was performed in the 2nd week of August, 2022 at Coimbatore, Tamlinadu, India.

3. Results and Discussion

3.1. XRD Analysis

The crystalline nature of the obtained samples of NiS, CdS, Ni–Cd–S and Ni–Cd–S/rGO was measured using X-ray diffraction pattern and presented in Figure 1. The XRD pattern of the pristine photocatalysts NiS and CdS, displayed in Figure 1a–c. The

diffraction peaks of NiS confirmed as rhombohedral structure (JCPDS: 12-0041) [25] with cell parameters of $a = 9.620 \text{ \AA}$, $c = 3.149 \text{ \AA}$. The diffraction pattern of the NiS identified at $2\theta = 30.31^\circ$, 32.20° , 35.69° , 37.34° , 40.45° , 48.84° , 50.14° and 52.64° with corresponding planes of (1 0 1), (3 0 0), (0 2 1), (2 2 0), (2 1 1), (1 3 1), (4 1 0), and (4 0 1), respectively.

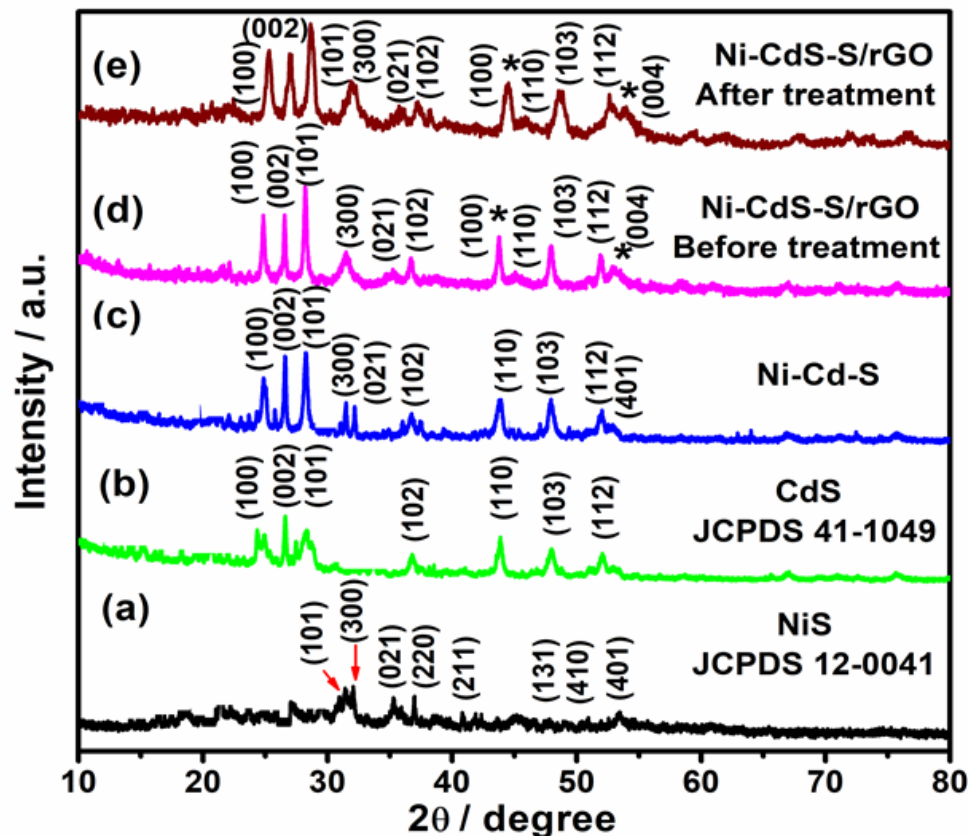


Figure 1. XRD patterns of (a) NiS, (b) CdS, (c) Ni-Cd-S and (d) Ni-Cd-S/rGO nanocomposite before photocatalyst treatment and (e) Ni-Cd-S/rGO nanocomposite after photocatalyst treatment.

The XRD pattern of the CdS has the hexagonal structure (JCPDS 41-140) [26] with cell parameters of $a = 4.140 \text{ \AA}$, $b = 4.143 \text{ \AA}$ and $c = 6.719 \text{ \AA}$. The corresponding planes for the diffraction are observed at 24.87° , 26.52° , 28.20° , 36.65° , 43.71° , 47.88° with the planes of 50.92° are (1 0 0), (0 0 2), (1 0 1), (1 0 2), (1 1 0), (1 0 3) and (1 1 2), respectively. The XRD pattern for nanocomposite Ni-Cd-S shows that mixed crystal structure of rhombohedral and hexagonal. The strong diffraction pattern depicts good crystalline nature of the product. The peaks (2θ) values at 18.44° , 24.82° , 26.52° , 28.20° , 32.20° , 35.69° , 36.50° , 43.71° , 47.88° , 51.86° and 52.64° are corresponding planes of (1 1 0), (1 0 0), (0 0 2), (1 0 1), (3 0 0), (0 2 1), (1 0 2), (1 1 0), (1 0 3), (1 1 2) and (4 0 1). Because of the size difference between the ions Cd^{2+} and Ni^{2+} , there is little compressive micro strain in the lattice, which causes peak broadening and peak shifts in the reflection planes [27]. Similarly, the XRD pattern for Ni-Cd-S and Ni-Cd-S/rGO, shows mixed crystalline faces of the NiS and CdS. Figure 1d,e represents the XRD pattern of Ni-Cd-S/rGO nanocomposite before and after photocatalysts treatment. No additional peaks were observed for the treated sample, it indicates the catalyst possess high structural stability. In addition to that, two additional peaks (marked by “*”) are identified in Ni-Cd-S/rGO pattern, which is assigned to rGO, the 2θ values are at 42.50° and 52.55° corresponding planes of (1 0 0) and (0 0 4). It is well confirmed that the nanocomposite is evenly distributed on the graphite sheet, which is further confirmed by HR-SEM and HR-TEM images. The identified crystal structure of the Ni-Cd-S/rGO

nanocomposite is mixed phases of rhombohedral and hexagonal structure. The crystallite size of the composite was calculated using Debye-Scherrer's formula [28].

$$D = (k\lambda/\beta\cos\theta) \quad (3)$$

where D represents particle size, $K = 0.95$ (constant) and β denotes full width at half maximum (FWHM). The calculated size of NiS, CdS, Ni-Cd-S and Ni-Cd-S/rGO are 15 nm, 13 nm, 20 nm and 18 nm, respectively. The diffraction planes of Ni-Cd-S/rGO nanocomposite exhibit more sharp peaks than the NiS, CdS and Ni-Cd-S. The reason behind this is that the nanoparticle (Cd and S) completely covers over the Ni (atomic radius is 0.124 nm) particle, so the diffraction takes place over the other compound, and as a result, more peaks appear in the composite.

3.2. FTIR Analysis

The FTIR spectra of the NiS, CdS, Ni-Cd-S and Ni-Cd-S/rGO nanocomposite is in the range of 500–4000 cm^{-1} , shown in Figure S1. The peaks illustrated in Figure S1a, at about 1098, 753 and 635 cm^{-1} , correspond to Ni-S functional group [29]. Similarly, the band at 1622 cm^{-1} belongs to groups of H_2O , while the band at 1383 cm^{-1} could likely originate from contaminant carbon. The absorption peaks of 2931 and 3023 cm^{-1} were ascribed to the C-H stretching mode of vibration [30–32]. The peaks at 2857 and 1742 cm^{-1} can be assigned to the C-O bond originating from the adsorption of CO_2 (from the atmosphere) and the band at 3394 cm^{-1} were ascribed to the vibration of the O-H group. The absorption peaks (Figure S1b) observed at 528 and 721 cm^{-1} in are assigned to stretching vibrations of Cd-S. The appearance of the strong peaks at 906 to 1094 cm^{-1} is assigned to C-O stretching vibration. The observed peaks at 1397 to 2915 cm^{-1} correspond to the functional group of C-S, the appearance of this functional group is due to the high amount of thiourea presented in the synthesized sample. The spectrum displays a band at 3023 and 3382 cm^{-1} assigned to O-H stretching of absorbed water molecules on the surface of CdS [33].

In the Ni-Cd-S and Ni-Cd-S/rGO nanocomposites in Figure S1c,d, the vibrational band at 635 cm^{-1} is assigned to Ni-S, and a weak bond for Cd^{2+} interaction is noticed at 721 cm^{-1} . The stretching vibration of the strong bond obtained at 1098 cm^{-1} is due to the presence of C-O, and N-H bending vibrations are observed in the range from medium to strong intensity 1146 to 1639 cm^{-1} . The C-C stretching vibrations occurred in the range between 2085 to 2915 cm^{-1} [34]. The O-H groups at 3441 cm^{-1} are observed and believed to be attached on the surface of the prepared photocatalysts. Also, the FTIR spectrum of rGO exhibited stretching frequency of hydroxyl, alkoxy and O-H bending at 3441, 2915, 2847 and 139 cm^{-1} [29]. This is due to coordination bond between the Cd, Ni and sulfide ions. These results provide the efficient electron transportation to enhance the charge separation and improve the optical characteristic of prepared photocatalysts.

3.3. Morphological Analysis

The morphologies of the synthesized catalysts of NiS, CdS, Ni-Cd-S and Ni-Cd-S/rGO (Figure 2a–l) are further characterized through HR-SEM with EDS and HR-TEM images. As depicted in (Figure 2a–f), the HR-SEM images of pure NiS and CdS, respectively, it clearly shows uniform nanostructures connected with each other's. Subsequently, the Ni-Cd-S and Ni-Cd-S/rGO nanocomposite are shown in (Figure 2g–l). The high and low magnification HR-SEM images were performed to understand the morphology of the nanocomposite [35]. The showed HR-SEM images with aggregation, which is due to the small size of the particles in nanoscale. Therefore, the high surface area of the particles in the nanoscale connected to each other due to high surface energy. The combined Ni-Cd-S and Ni-Cd-S/rGO nanocomposite exhibited self-assembled and accumulated nanospheres with smooth area. The highly magnified images also validated that the agglomerated nanospheres can be broadly distributed on the surface of Ni-Cd-S and Ni-Cd-S/rGO nanocomposite to form a well fined structure [36,37]. In addition, the more detailed interfacial morphology and structure of Ni-Cd-S/rGO are investigated by HR-

TEM images. Figure 3a,b shows the homogeneous distribution of NiS and CdS on the surface of Ni–Cd–S/rGO. Further detailed observations of nanocomposite in Figure 3c–i images verify the formation of thin and transparent sheets of layered nanosheet [38] type morphology of rGO. The well-dispersed rGO induces the enhancement in conductivity of ions inside the sample. More clearly, the selected area electron diffraction (SAED) pattern in Figure 3j exhibits the diffraction dot matrix of high crystalline Ni–Cd–S/rGO nanocomposite [39].

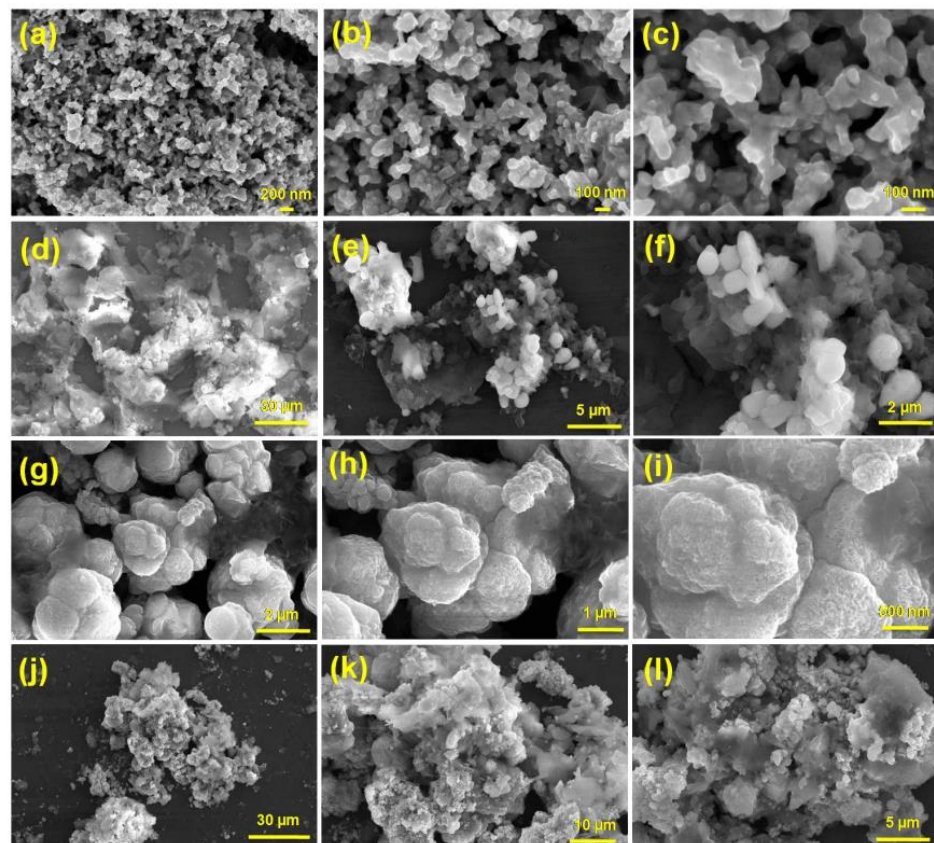


Figure 2. HR-SEM images of (a–c) NiS, (d–f) CdS, (g–i) Ni–Cd–S and (j–l) Ni–Cd–S/rGO nanocomposite.

3.4. XPS Analysis

The elemental chemical states of Ni–Cd–S/rGO nanocomposite were further investigated by XPS. Figure 4a shows the survey spectrum of Ni–Cd–S/rGO nanocomposite, which confirms that the nanocomposite contains Cd, Ni, C, S and O elements. The major intensity peak for C 1s (Figure 4b) positioned at 284.8 eV is ascribed to Sp^2 carbon present in graphitic structure, while the other two peaks at 286.1 eV and 288.5 eV are assigned to C–O and COO- functional groups, respectively [40]. The presence of these peaks is in good agreement with the previously reported studies [41]. The peaks positioned at 876.2 eV and 856.3 eV are assigned to $2p_{1/2}$ and $2p_{3/2}$ of Ni^{2+} (Figure 4e) [42]. For O 1s (Figure 4c), the peak at 531.6 eV is due to the residual oxygen containing group that bonded with the C atoms presented in rGO. For the S 2p spectrum (Figure 4f), the peaks positioned at 163.1 eV and 161.7 eV are fitted to S $2p_{1/2}$ and S $2p_{3/2}$, respectively [43]. There is a satellite peak located at 168.6 eV due to the strong interaction of the S–O bond [44]. The high-resolution spectra of Cd 3d (Figure 4d) with binding energy at 412.1 eV and 405.4 eV correspond to Cd $3d_{3/2}$ and Cd $3d_{5/2}$, respectively. The other two peaks are assigned to satellite peaks. The binding energy difference between $3d_{3/2}$ and $3d_{5/2}$ is close to 6.7 eV, confirming that Cd has a +2-oxidation state [45]. The results obtained from XPS confirm the formation of the Ni–Cd–S/rGO nanocomposite.

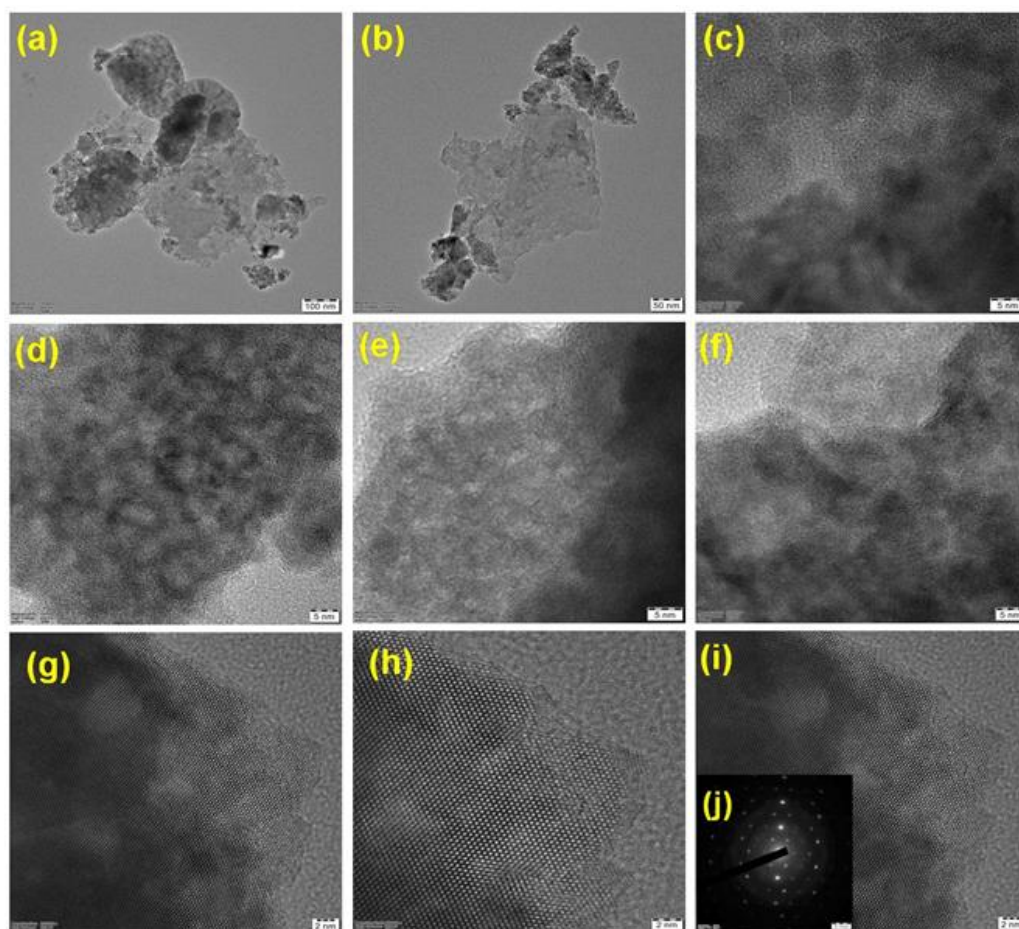


Figure 3. HRTEM images of (a–i) Ni–Cd–S/rGO nanocomposite and insert of (j) corresponding SAED pattern of Ni–Cd–S/rGO nanocomposite (inset of figure (i)).

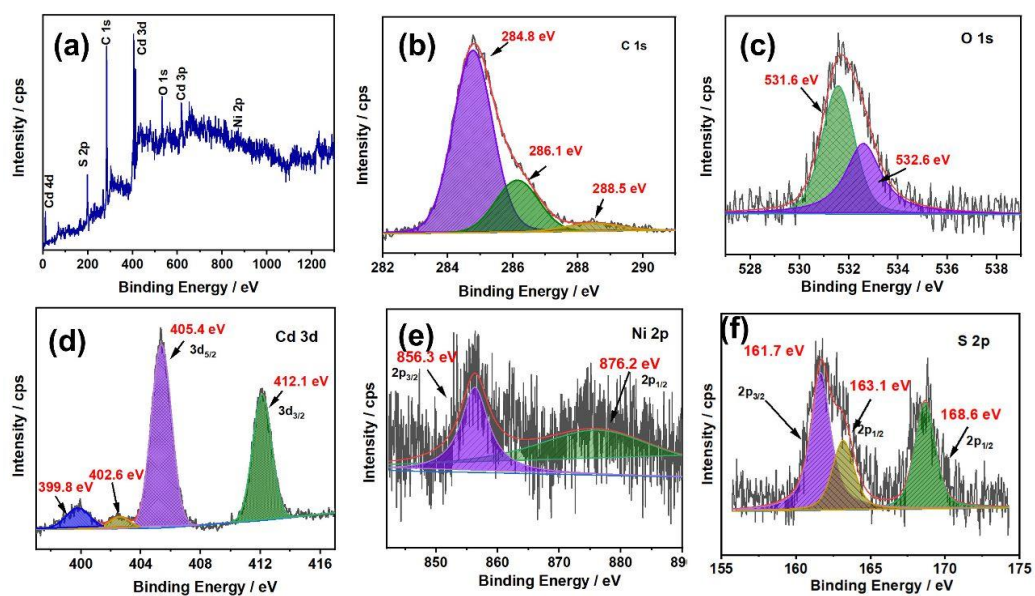


Figure 4. (a) XPS survey spectrum of Ni–Cd–S/rGO nanocomposite and (b–f) are the high-resolution elements C, O, Cd, Ni and S, respectively.

3.5. Optical Property

The optical properties of the photocatalysts were investigated by UV-Vis spectroscopy. To examine the optical absorption properties and energy band gaps of NiS, CdS, Ni-Cd-S and Ni-Cd-S/rGO photocatalysts, UV-Vis recorded and displayed the spectra in Figure 5a,b. The absorption edges of photocatalysts are shown in the visible region between 444 and 510 nm as presented in Figure 5a. Based on the absorption spectra [46], the bandgap energy (E_g) of the photocatalysts was measured from Tauc equation [47].

$$(\alpha h\nu)^{1/2} = \beta(h\nu - E_g) \quad (4)$$

In this equation, β is the indirect bandgap constant, whereas α and $h\nu$ stand for the optical absorption coefficient and planck constant. Figure 5b shows the determined bandgap values for NiS, CdS, Ni-Cd-S and Ni-Cd-S/rGO of 2.44 eV, 3.05 eV, 3.28 eV and 2.79 eV, respectively. So, the developed Ni-Cd-S/rGO nanocomposite showed superior optical properties, which can be increased photocatalytic function [48].

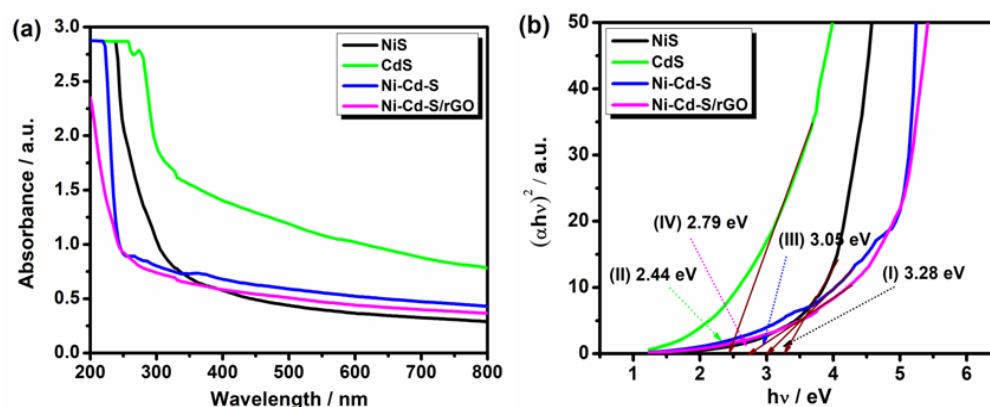


Figure 5. (a) UV-vis spectra of NiS, CdS, Ni-Cd-S and Ni-Cd-S/rGO. (b) Bandgap energy of (I) NiS, (II) CdS, (III) Ni-Cd-S and (IV) Ni-Cd-S/rGO.

3.6. Photocatalytic Activity

As a contagious organic pollutant, the MB dye is carcinogenic to the environment. As a result, we chose to study the photocatalytic degradation of synthesized materials, such as NiS, CdS, Ni-Cd-S and Ni-Cd-S/rGO nanocomposite, under a visible light region. The lowest and highest value of the UV-Vis spectra of the MB dye in the presence of photocatalysts (NiS, and Ni-Cd-S/rGO) are shown in Figure 6a,b, and the remaining CdS and Ni-Cd-S are presented in Figure S2a,b. When the MB dye solution was light irradiated, the dye concentration decreased as the visible light irradiation duration increased, resulting in the breakdown of the MB dye's degradation [49]. The NiS, CdS, Ni-Cd-S and Ni-Cd-S/rGO nanocomposite decompose the organic molecules within 2.5 h, with efficiencies of about 90%, 89%, 91% and 94%, respectively.

The nanocomposite structure enhanced degradation efficiency by increasing the light absorption rate, electron hole pair production and recombination delay. Ni-Cd-S/rGO nanocomposite out performed NiS, CdS and Ni-Cd-S photocatalysts interms of degradation rates. Figure 7a depicts the changes in initial and final dye concentrations in the presence and absence of photocatalyst versus light irradiation with respect to time (t) for the MB dye [50]. A large amount of reactive oxygen species (ROS) are generated based on sub energy level of the conduction band. In addition to the pseudo-first order kinetics experiments shown in Figure 7b, the degradation rates of NiS, CdS, Ni-Cd-S and Ni-Cd-S/rGO nanocomposite against MB dye are 0.024 min^{-1} , 0.024 min^{-1} , 0.025 min^{-1} and 0.034 min^{-1} , respectively. The rate constant value and R^2 values from the experiments are provided in Figure 7b.

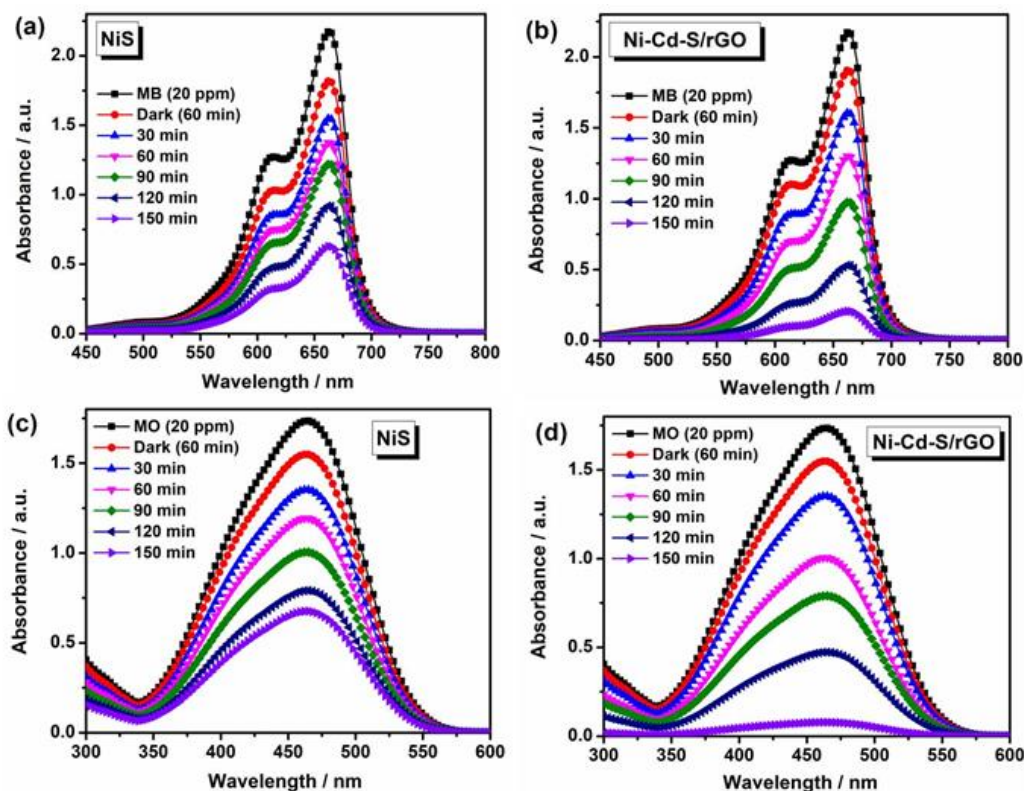


Figure 6. The lowest and highest photocatalytic degradation UV spectrum of (a) NiS, (b) Ni-Cd-S/rGO for MB dye and (c) NiS and (d) Ni-Cd-S/rGO for MO dye.

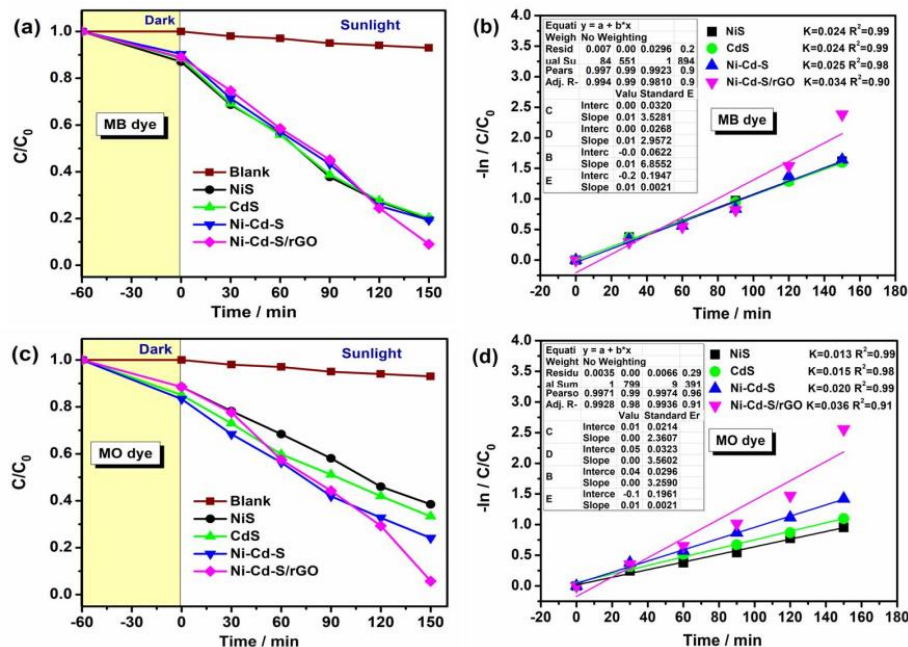


Figure 7. (a) Photocatalytic degradation of MB under sunlight irradiation and (b) corresponding first-order kinetic plots. (c) Photocatalytic degradation of MO under visible-light irradiation and (d) corresponding first-order kinetic plots of NiS, CdS, Ni-Cd-S and Ni-Cd-S/rGO nanocomposite, respectively.

Likewise, the photocatalytic dye degradation reaction with NiS, CdS, Ni-Cd-S and Ni-Cd-S/rGO nanocomposite was performed against another model pollutant of lowest and higher value of MO dye, the results displayed in Figure 6c,d and the other CdS and

Ni–Cd–S photocatalyst are shown in Figure S2c,d. Within 2.5 h, the degradation efficiency of the NiS, CdS, Ni–Cd–S and Ni–Cd–S/rGO were reached around 78.1%, 81.3%, 86.2% and 97.1%, respectively, under the identical experimental conditions. In terms of degradation rates, Ni–Cd–S/rGO nanocomposite beat the bare NiS, CdS, and Ni–Cd–S photocatalysts. For the MO dyes, Figure 7c depicts the changes in initial and final dye concentrations with respect to time (t) in the presence and absence of photocatalyst vs. light irradiation [51]. Based on the sub energy level of the conduction band, a huge number of ROS are produced. The degradation rates of NiS, CdS, Ni–Cd–S and Ni–Cd–S/rGO nanocomposite against MO dye were 0.013 min^{-1} , 0.015 min^{-1} , 0.020 min^{-1} and 0.036 min^{-1} , respectively. In addition, the pseudo-first order kinetics experiments reported in Figure 7d. The rate constant value and R^2 values from the experiments are provided in Figure 7d. Compared with the reported data in Table 1, the prepared Ni–Cd–S/rGO photocatalysis exhibit remarkably excellent dye degradation performance [52–55].

Table 1. Comparison of current and reported studies of NiS, CdS, Ni–Cd–S and Ni–Cd–S/rGO nanocomposites in Methylene Blue and Methyl Orange dye.

Catalyst	Light Source	Dye	Dye Concentration (mg L ⁻¹)	Irradiation Time	Efficiency (%)	Ref.
TiO ₂ NTs/CdS–CuS (8%)	Solar	MB, MO	1 mol/L	6 h	89.28, 63.36	[18]
Ag–CdS@Pr–TiO ₂ core/shell Nanoparticles	Visible light	MO	0.0049 g	30 min	98	[19]
NiS/Ag ₂ MoO ₄	Visible light	MB	10	140 min	90.8	[20]
3D/2D TiO ₂ /p–g–C ₃ N ₄	Visible light	MO	10	4 h	99	[24]
K ₂ Ti ₆ O ₁₃ Nanobelt	UV	MB	10	120 min	82.1	[47]
ZnTiO ₃ /g–C ₃ N ₄	Visible light	MO	10	180 min	76	[52]
Sn-doped CdS NPs	Sunlight	MB	20	180 min	97.5	[53]
NiS/analcime	Visible light	MB	10	180 min	88.76	[54]
Zn doped NiS QDs	Visible light	MB	10	2 h	78	[55]
Ni–Cd–S/rGO	Sunlight	MO	25	150 min	97	This work

The process of heterogeneous photocatalytic dye degradation consists of two steps: (i) dye molecules interact with the catalyst (surface adsorption), and (ii) photodegradation of the dye begins. As a result, the photocatalytic system is highly reliant on the catalyst's adsorption and photodegradation capabilities [56]. Because the Ni–Cd–S/rGO nanocomposites had the highest degradation efficiency among all catalysts, they were solely chosen for the scavenger investigation to better understand the degradation mechanism. In general, in photodegradation experiments, the pollutants are oxidized by some reactive oxygen species, such as holes, hydroxyl radicals and superoxide radicals (h^+ , $OH\bullet$, and $O_2\bullet^-$), respectively. The radical experiment was performed to identify the reactive species involved in the photodegradation of MB and MO dye by Ni–Cd–S/rGO with various kinds of radical scavengers with the same concentration, such as benzoquinone (BQ), ethylene diamine tetra acetic acid (EDTA) and methanol, and the obtained results are depicted in Figure 8a. As a result, the h^+ , $OH\bullet$, and $O_2\bullet^-$ are eliminated by accumulation of related scavengers, such as methanol ($OH\bullet$ scavenger), EDTA (h^+ scavenger), and BQ ($O_2\bullet^-$ scavenger) into reaction solution, respectively [57]. In the scavenger experiments, the BQ only demonstrates significant differences in efficiency of both dyes. As a result, superoxide radicals play an important role in total photodegradation efficiency.

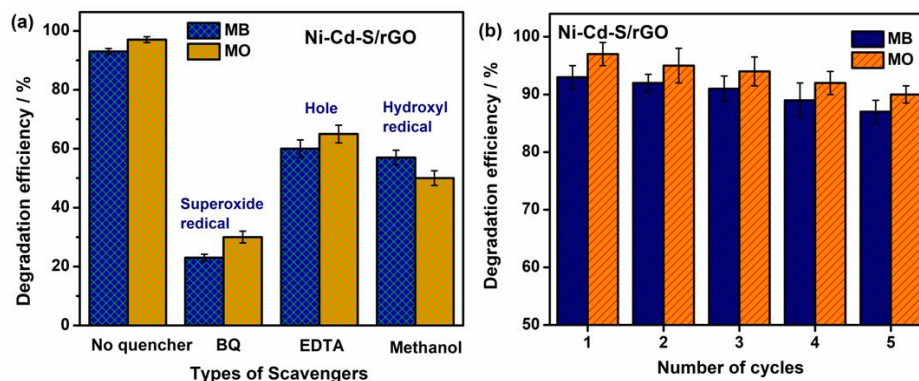
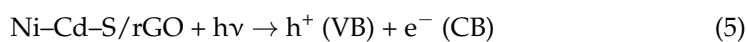


Figure 8. (a) Scavengers' studies and (b) reusability study of Ni–Cd–S/rGO nanocomposite for MB and MO dye.

Furthermore, the stability and reusability of Ni–Cd–S/rGO nanocomposite is important for the promotion of the catalyst for industrial application [58]. In every cycle, the recovered material was washed and centrifuged. Then, the recovered material was weighed again to add the lost amount and used for the next cycle. As shown in Figure 8b, the photodegradation efficiency of Ni–Cd–S/rGO nanocomposite for the degradation of MO almost remained same even after five cycles, which shows that the prepared nanocomposite is reusable. The mechanism of dye degradation for the Ni–Cd–S/rGO nanocomposite catalyst is described as follows.

(i) Formation of exciton (electron hole pair)



(ii) Formation of hydroxyl radicals



(iii) Formation of superoxide radicals



(iv) Photo degradation of FG and RB dye



In this work, the Ni–Cd–S/rGO nanocomposite outperforms the NiS, CdS and Ni–Cd–S photocatalysts. The increased efficiency of the Ni–Cd–S/rGO nanocomposite may be attributed to three important factors: (i) a reduction in band gap energy and (ii) photocatalyst shape (iii) adsorption behavior (Catalyst pollutant interaction). Unambiguously, the Ni–Cd–S/rGO nanocomposites band gap energy [59,60] was lower at 2.79 eV compared to other prepared metal composites. In this regard, the Ni–Cd–S/rGO catalyst has higher photocatalytic activity due to increased absorption of incoming visible light and decreased recombination. Furthermore, the shape of the Ni–Cd–S/rGO fused heterostructure aids in dye molecule interaction. In addition, Figure 9a,b shows the error bar diagram of the effect of sunlight intensity on the degradation of MB and MO dyes with respect to the degradation ration of C/C_0 and various time intervals (t). There is no photocatalytic degradation of MB, and MO is noticed in the absence of the photocatalyst (blank) at less than 60 min in a dark environment, and illumination conditions occur in the process of natural sunlight. Among the four photocatalysts, Ni–Cd–S/rGO shows the best results to degrade MO dye molecules, achieving degradation within 150 min under sunlight irradiation. The

error bar results clearly show that the sample can be performed with high reproducibility. In order to understand the morphological stability of the sample, after the five cycles of the degradation process, HRTEM analysis was performed. Figure 10a–e shows different morphology of retrieved Ni–Cd–S/rGO catalyst, and the corresponding SAED pattern is shown in Figure 10f. Interestingly, no significant morphological variation was observed even after five subsequent cycles. It clearly indicates good structural stability of the catalyst as confirmed in Figure 1.

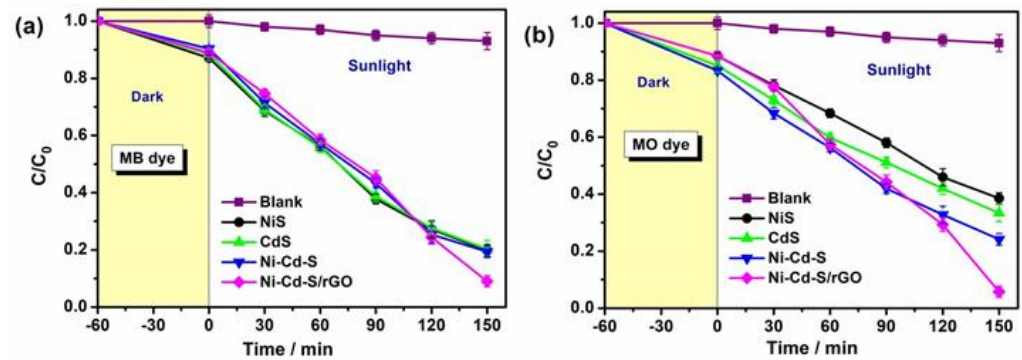


Figure 9. Error bar determination of photocatalytic degradation of (a) MB and (b) MO dyes under sunlight irradiation of NiS, CdS, Ni–Cd–S and Ni–Cd–S/rGO nanocomposite, respectively.

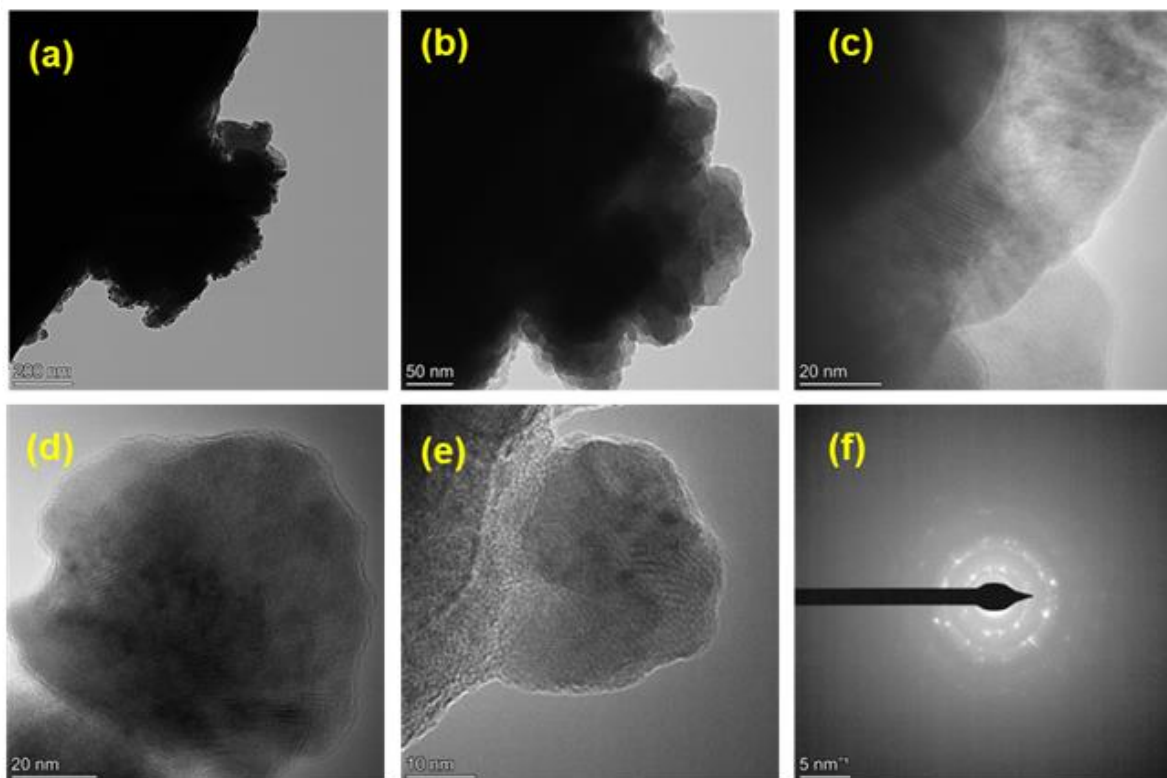
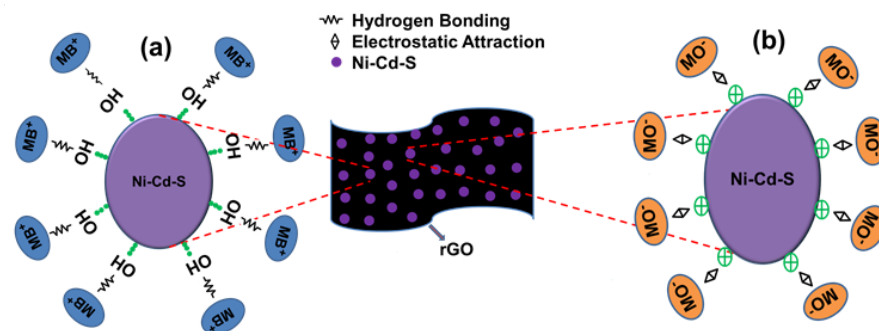


Figure 10. (a–e) HRTEM images with different magnifications and (f) corresponding SAED pattern of the retrieved Ni–Cd–S/rGO catalyst.

3.7. Possible Mechanism of Photocatalysis for Selective dye Adsorption Degradation

The best photocatalytic performance of Ni–Cd–S/rGO nanocomposite for selective cationic (MB) and anionic dye (MO) adsorption mechanism is illustrated in Scheme 1. High surface area of rGO can effectively interconnect with the cauliflower structures of Ni–Cd–S nanoparticles, which could significantly enhance the contact opportunity of dye molecules on the Ni–Cd–S/rGO surface [61]. The selective cationic and anionic dye

adsorption performance of Ni–Cd–S/rGO nanocomposite was mainly dependent on the surface and structure of the prepared photocatalyst and the intrinsic features of targeted pollutants. The MB dye molecules have larger adsorption capacity compared with MO dye molecules. Because the chemical composition of the dyes may also affect the corresponding adsorption performance. The adsorption property of Ni–Cd–S/rGO could be connected with the formation of hydrogen bonding (OH) interactions between MB dye molecules and electrostatic attraction between MO dye molecules as shown in Scheme 1a,b, respectively.



Scheme 1. Proposed adsorption model for (a) MB cationic dye and (b) MO anionic dye on the surface of Ni–Cd–S/rGO nanocomposite.

4. Conclusions

In summary, pristine NiS, CdS, Ni–Cd–S and Ni–Cd–S/rGO nanocomposite have been successfully synthesized by a hydrothermal method. The crystal structure, morphology and composition of elements were confirmed by advanced characterization techniques. The textile dyes MB and MO were successfully degraded under visible light irradiation. Among the prepared photocatalysts, Ni–Cd–S/rGO nanocomposite displays the most efficient dye degradation performance. The photocatalytic dye degradation efficiency of 94% and 97.1% were achieved for MB and MO dyes, respectively, under sunlight irradiation. The photocatalytic enhancement can be ascribed to quickly transferring the photogenerated carriers and reducing electron and hole pair recombination. In addition to this, this research could shed new light on the synergetic effect of Ni and Cd. The novel nanocomposites are regarded as a promising photocatalysts for the degradation of various textile pollutants.

Supplementary Materials: The following supporting information can be downloaded at: <https://www.mdpi.com/article/10.3390/su142316184/s1>. Figure S1. FTIR spectra of (a) NiS, (b) CdS, (c) Ni–Cd–S and (d) Ni–Cd–S/rGO nanocomposite. Figure S2. The lowest and highest Photocatalytic degradation UV spectrum of (a) CdS, (b) Ni–Cd–S for MB dye and (c) CdS and (d) Ni–Cd–S for MO dye.

Author Contributions: Conceptualization, N.K. and G.M.; methodology, N.K.; software, K.K.; validation, G.M., R.K.M. and T.K.; formal analysis, T.K. and R.K.M.; investigation, N.K. and G.M.; writing—original draft preparation, N.K. and G.M.; writing—review and editing, N.K. and G.M.; supervision, G.M. All authors have read and agreed to the published version of the manuscript.

Funding: This research received no external funding.

Institutional Review Board Statement: Not applicable.

Informed Consent Statement: Not applicable.

Data Availability Statement: Not applicable.

Acknowledgments: The author (G. Murugadoss) acknowledges the management of Sathyabama Institute of Science and Technology, Chennai, Tamilnadu, India for providing lab facilities and support. One of the authors, Rajesh Kumar Manavalan thanks the contract no. 40/is2 and gratefully acknowledges research funding from the Ministry of Science and Higher Education of the Russian Federation (Ural Federal University project within the Priority 2030 Program).

Conflicts of Interest: The authors declare no conflict of interest.

References

1. Mathon, B.; Coquery, M.; Miede, C.; Vandycke, A.; Choubert, J.-M. Influence of water depth and season on the photodegradation of micropollutants in a free-water surface constructed wetland receiving treated wastewater. *Chemosphere* **2019**, *235*, 260–270.
2. Salari, H.; Sadeghinia, M. MOF-templated synthesis of nano Ag₂O/ZnO/CuO heterostructure for photocatalysis. *J. Photochem. Photobiol. A Chem.* **2019**, *376*, 279–287. [[CrossRef](#)]
3. Liu, Y.; Zhang, Q.; Xu, M.; Yuan, H.; Chen, Y.; Zhang, J.; Luo, K.; Zhang, J.; You, B. Novel and efficient synthesis of Ag-ZnO nanoparticles for the sunlight induced photocatalytic degradation. *Appl. Surf. Sci.* **2019**, *476*, 632–640. [[CrossRef](#)]
4. Peera, S.G.; Koutavarapu, R.; Chao, L.; Singh, L.; Murugadoss, G.; Rajeshkhanna, G. 2D MXene Nanomaterials as Electrocatalysts for Hydrogen Evolution Reaction (HER): A Review. *Micromachines* **2022**, *13*, 1499. [[CrossRef](#)] [[PubMed](#)]
5. Lai, C.; Zhang, M.M.; Lia, B.S.; Huang, D.L.; Zeng, G.M.; Qin, L.; Liu, X.G.; Yi, H.; Cheng, M.; Li, L.; et al. Fabrication of CuS/BiVO₄ (040) binary heterojunction photocatalysts with enhanced photocatalytic activity for Ciprofloxacin degradation and mechanism insight. *Chem. Eng. J.* **2019**, *358*, 891–902. [[CrossRef](#)]
6. Liu, X.W.; Xua, J.J.; Ni, Z.Y.; Wang, R.C.; You, J.H.; Guo, R. Adsorption and visible light-driven photocatalytic properties of Ag₃PO₄/WO₃composites: A discussion of the mechanism. *Chem. Eng. J.* **2019**, *356*, 22–33. [[CrossRef](#)]
7. Zhang, B.; Wang, Q.; Zhuang, J.; Guan, S.; Li, B. Molten salt assisted in-situ synthesis of TiO₂/g-C₃N₄ composites with enhanced visible-light-driven photocatalytic activity and adsorption ability. *J. Photochem. Photobiol. A Chem.* **2018**, *362*, 1–13. [[CrossRef](#)]
8. Wang, Q.; Li, B. Flux Growth of Highly Crystalline Photocatalytic BaTiO₃ Particle Layers on Porous Titanium Sponge Substrate and Insights into the Formation Mechanism. *IOP Conf. Ser. Mater. Sci. Eng.* **2017**, *239*, 012013. [[CrossRef](#)]
9. Murugadoss, G.; Thirupathi, K.; Venkatesh, N.; Hazra, S.; Mohankumar, A.; Thirupathi, G.; Kumar, M.R.; Sundararaj, P.; Rajabathar, J.R.; Sakthivel, P. Construction of novel quaternary nanocomposite and its synergistic effect towards superior photocatalytic and antibacterial application. *J. Environ. Chem. Eng.* **2022**, *10*, 106961.
10. Alomar, M.; Liu, Y.L.; Chen, W.; Fida, H. Controlling the growth of ultrathin MoS₂ nanosheets/CdS nanoparticles by two-step solvothermal synthesis for enhancing photocatalytic activities under visible light. *Appl. Surf. Sci.* **2019**, *480*, 1078–1088. [[CrossRef](#)]
11. Lv, J.X.; Zhang, Z.M.; Wang, J.; Lu, X.L.; Zhang, W.; Lu, T.B. In situ synthesis of CdS/Graphdiyne heterojunction for enhanced photocatalytic activity of hydrogen production. *ACS Appl. Mater. Interfaces* **2019**, *11*, 2655–2661. [[CrossRef](#)] [[PubMed](#)]
12. Chen, Z.; Liu, S.Q.; Yang, M.Q.; Xu, Y.J. Synthesis of uniform CdS nanospheres/graphene hybrid nanocomposites and their application as visible light photocatalyst for selective reduction of nitro organics in water. *ACS Appl. Mater. Interfaces* **2013**, *5*, 4309–4319. [[CrossRef](#)] [[PubMed](#)]
13. Park, H.; Kim, Y.K.; Choi, W.Y. Reversing CdS preparation order and its effects on photocatalytic hydrogen production of CdS/Pt-TiO₂ hybrids under visible light. *J. Phys. Chem. C* **2011**, *115*, 6141–6148.
14. Shi, W.L.; Guo, F.; Li, M.Y.; Shi, Y.; Tang, Y.B. N-doped carbon dots/CdS hybrid photocatalyst that responds to visible/ near-infrared light irradiation for enhanced photocatalytic hydrogen production. *Sep. Purif. Technol.* **2019**, *212*, 142–149.
15. Wang, B.; He, S.; Zhang, L.L.; Huang, X.Y.; Gao, F.; Feng, W.H.; Liu, P. CdS nanorods decorated with inexpensive NiCd bimetallic nanoparticles as efficient photocatalysts for visible-light-driven photocatalytic hydrogen evolution. *Appl. Catal. B* **2019**, *243*, 229–235. [[CrossRef](#)]
16. Irfan, R.M.; Tahir, M.H.; Khan, S.A.; Shaheen, M.A.; Ahmed, G.; Iqbal, S. Enhanced photocatalytic H₂ production under visible light on composite photocatalyst (CdS/NiSe nanorods) synthesized in aqueous solution. *J. Colloid Interface Sci.* **2019**, *557*, 1–9. [[CrossRef](#)]
17. El-Katori, E.E.; Ahmed, M.A.; El-Bindary, A.A.; Oraby, A.M. Impact of CdS/SnO₂ heterostructured nanoparticle as visible light active photocatalyst for the removal methylene blue dye. *J. Photochem. Photobiol. A Chem.* **2020**, *392*, 12403.
18. Hou, J.; Huang, B.; Kong, L.; Xie, Y.; Liu, Y.; Chen, M.; Wang, Q. One-pot hydrothermal synthesis of CdS–CuS decorated TiO₂ NTs for improved photocatalytic dye degradation and hydrogen production. *Ceram. Int.* **2021**, *47*, 30860–30868. [[CrossRef](#)]
19. Singh, A.; Ahmed, A.; Sharma, A.; Sharma, C.; Paul, S.; Khosla, A.; Gupta, V.; Arya, S. Promising photocatalytic degradation of methyl orange dye via sol-gel synthesized Ag–CdS@Pr-TiO₂ core/shell nanoparticles. *Phys. B Condens. Matter.* **2021**, *616*, 413121.
20. Kokilavani, S.; Al-Kheraif, A.A.; Thomas, A.M.; Syed, A.; Elgorban, A.M.; Raju, L.L.; Das, A.; Khan, S.S. Novel NiS/Ag₂MoO₄ heterostructure nanocomposite: Synthesis, characterization and superior antibacterial and enhanced photocatalytic activity. *Phys. E Low Dimens. Syst. Nanostruct.* **2021**, *133*, 114767. [[CrossRef](#)]
21. Cheng, L.; Xiang, Q.J.; Liao, Y.L.; Zhang, H.W. CdS-Based photocatalysts. *Energy Environ. Sci.* **2018**, *11*, 1362–1391. [[CrossRef](#)]
22. Lia, L.; Wu, J.; Liu, B.B.; Liu, X.J.; Li, C.; Gong, Y.Y.; Huang, Y.L.; Pan, L.K. NiS sheets modified CdS/reduced graphene oxide composite for efficient visible light photocatalytic hydrogen evolution. *Catal. Today* **2018**, *315*, 110–116.
23. Xu, J.L.; Zhang, L.; Xu, G.C.; Sun, Z.P.; Zhang, C.; Ma, X.; Qi, C.L.; Zhang, L.; Jia, D.Z. Facile synthesis of NiS anchored carbon nanofibers for high-performance supercapacitors. *Appl. Surf. Sci.* **2018**, *434*, 112. [[CrossRef](#)]
24. Wang, Q.; Zhang, L.; Guo, Y.; Shen, M.; Wang, M.; Li, B.; Shi, J. Multifunctional 2D porous g-C₃N₄ nanosheets hybridized with 3D hierarchical TiO₂ microflowers for selective dye adsorption, antibiotic degradation and CO₂ reduction. *Chem. Eng. J.* **2020**, *396*, 125347. [[CrossRef](#)]

25. Murugadoss, G.; Kumar, M.R.; Kathalingam, A.; Rajabathar, J.R.; Al-Lohedan, H.; Al-Dhayan, D.M. Facile synthesis of heterostructure CeO₂/CdS and CdS/CeO₂ nanocomposites for photocatalytic application of methylene blue textile dye. *J. Ovonic Res.* **2021**, *17*, 595–603.
26. Ramalingam, G.; Magdalane, C.M.; Kumar, B.A.; Yuvakkumar, R.; Ravi, G.; Jothi, A.I.; Rotte, N.K.; Murugadoss, G.; Ananth, A. Enhanced visible light-driven photocatalytic performance of CdSe nanorods. *Environ. Res.* **2022**, *203*, 111855.
27. Muruganandam, S.; Parivathini, K.; Murugadoss, G. Effect of co-doped (Ni²⁺: Co²⁺) in CdS nanoparticles: Investigation on structural and magnetic properties. *Appl. Phys. A* **2021**, *127*, 1–9.
28. Narthana, K.; Durai, G.; Kuppusami, P.; Theerthagiri, J.; Sujatha, S.; Lee, S.J.; Choi, M.Y. One-step synthesis of hierarchical structured nickel copper sulfide nanorods with improved electrochemical supercapacitor properties. *Int. J. Energy Res.* **2021**, *45*, 9983–9998.
29. Murugadoss, G.; Prakash, J.; Kumar, M.R.; Allothman, A.A.; Habila, M.A.; Peera, S.G. Controlled Synthesis of Europium-Doped SnS Quantum Dots for Ultra-Fast Degradation of Selective Industrial Dyes. *Catalyst* **2022**, *12*, 1128. [[CrossRef](#)]
30. Fazli, Y.; Pourmortazavi, S.M.; Kohsari, I.; Sadeghpur, M. Electrochemical synthesis and structure characterization of nickel sulfide nanoparticles. *Mater. Sci. Semicond. Process.* **2014**, *27*, 362–367. [[CrossRef](#)]
31. Jansi Rani, B.; Dhivya, N.; Ravi, G.; Zance, S.S.; Yuvakkumar, R.; Hong, S.I. Electrochemical performance of β-NiS@Ni(OH)₂ nanocomposite for water splitting applications. *ACS Omega* **2018**, *4*, 10302–10310. [[CrossRef](#)] [[PubMed](#)]
32. Liang, D.; Gao, J.; Sun, H.; Chen, P.; Hou, Z.; Zheng, X. Selective oxidation of glycerol with oxygen in a base-free aqueous solution over MWNTs supported Pt catalysts. *Appl. Catal. B Environ.* **2011**, *106*, 423–432.
33. Manikandan, A.; Hema, E.; Durka, M.; Selvi, M.A.; Alagesan, T.; Antony, S.A. Mn²⁺ doped NiS (Mn_xNi_{1-x}S: X = 0.0, 0.3 and 0.5) nanocrystals: Structural, morphological, opto-magnetic and photocatalytic properties. *J. Inorg. Organomet. Polym. Mater.* **2015**, *25*, 804–815.
34. Ponnaiah, S.K.; Prakash, P.; Vellaichamy, B. A new analytical device incorporating a nitrogen doped lanthanum metal oxide with reduced graphene oxide sheets for paracetamol sensing. *Ultrason. Sonochem.* **2018**, *44*, 196–203. [[CrossRef](#)] [[PubMed](#)]
35. Pal, D.B.; Rathoure, A.K.; Singh, A. Investigation of surface interaction in rGO-CdS photocatalyst for hydrogen production: An insight from XPS studies. *Int. J. Hydrog. Energy* **2021**, *46*, 26757–26769. [[CrossRef](#)]
36. Murugadoss, G.; Kandhasamy, N.; Kumar, M.R.; Alanazi, A.K.; Khan, F.; Salhi, B.; Yadav, H.M. Role of the dopant (silver) inclusion on before and after core metal-oxide reaction: Application on textile dyes removal. *Inorg. Chem. Commun.* **2022**, *137*, 109186. [[CrossRef](#)]
37. Liu, X.; Bie, C.; He, B.; Zhu, B.; Zhang, L.; Cheng, B. 0D/2D NiS/CdS nanocomposite heterojunction photocatalyst with enhanced photocatalytic H₂ evolution activity. *Appl. Surf. Sci.* **2021**, *554*, 149622. [[CrossRef](#)]
38. Jayaraman, V.; Mani, A. Ag, Ni bimetallic supported g-C₃N₄ 2D/Cd₂Sb₂O_{6.8} pyrochlore interface photocatalyst for efficient removal of organic pollutants. *J. Mater. Sci. Mater. Electron.* **2020**, *31*, 11247–11267.
39. Zhang, H.; Yu, Z.; Jiang, R.; Hou, Y.; Huang, J.; Zhu, H.; Yang, F.; Li, M.; Li, F.; Ran, Q. Metal organic frameworks constructed heterojunction with α-NiS-β-NiS/CdS: The effect of organic-ligand in UiO-66 for charge transfer of photocatalytic hydrogen evolution. *Renew. Energy* **2021**, *168*, 1112–1121. [[CrossRef](#)]
40. Muninathan, S.; Arumugam, S. Enhanced photocatalytic activities of NiS decorated reduced graphene oxide for hydrogen production and toxic dye degradation under visible light irradiation. *Int. J. Hydrogen Energy* **2021**, *46*, 6532–6546.
41. Some, S.; Kim, Y.; Yoon, Y.; Yoo, H.; Lee, S.; Park, Y.; Lee, H. High-quality reduced graphene oxide by a dual-function chemical reduction and healing process. *Sci Rep.* **2013**, *3*, 1–5. [[CrossRef](#)] [[PubMed](#)]
42. Hamid, A.A.A.; Yang, X.; Yang, J.; Chen, X.; Ying, J.Y. Graphene-wrapped nickel sulfide nanoprisms with improved performance for Li-ion battery anodes and supercapacitors. *Nano Energy* **2016**, *26*, 425–437.
43. Liu, G.; Thummavichai, K.; Lv, X.; Chen, W.; Lin, T.; Tan, S.; Zeng, M.; Chen, Y.; Wang, N.; Zhu, Y. Defect-Rich Heterogeneous MoS₂/rGO/NiS Nanocomposite for Efficient pH-Universal Hydrogen Evolution. *J. Nanomater.* **2021**, *11*, 662. [[CrossRef](#)] [[PubMed](#)]
44. Zhao, G.; Zhang, Y.; Yang, L.; Jiang, Y.; Zhang, Y.; Hong, W.; Tian, Y.; Zhao, H.; Hu, J.; Zhou, L.; et al. Nickel Chelate Derived NiS₂ Decorated with Bifunctional Carbon: An Efficient Strategy to Promote Sodium Storage Performance. *Adv. Funct. Mater.* **2018**, *28*, 1803690.
45. Alhammad, M.R.; Minnam Reddy, V.R.; Gedi, S.; Park, H.; Sayed, M.S.; Shim, J.J.; Kim, W.K. Performance of Graphene-CdS Hybrid Nanocomposite Thin Film for Applications in Cu(In,Ga)Se₂ Solar Cell and H₂ Production. *J. Nanomater.* **2020**, *10*, 245. [[CrossRef](#)] [[PubMed](#)]
46. Li, Z.; Wang, X.; Wang, X.; Lin, Y.; Meng, A.; Yang, L.; Li, Q. Mn-Cd-S@ amorphous-Ni₃S₂ hybrid catalyst with enhanced photocatalytic property for hydrogen production and electrocatalytic OER. *Appl. Surf. Sci.* **2019**, *491*, 799–806. [[CrossRef](#)]
47. Wang, Q.; Zhang, B.; Lu, X.; Zhang, X.; Zhu, H.; Li, B. Multifunctional 3D K₂Ti₆O₁₃ nanobelt-built architectures towards wastewater remediation: Selective adsorption, photodegradation, mechanism insight and photoelectrochemical investigation. *Catal. Sci. Technol.* **2018**, *8*, 6180–6195. [[CrossRef](#)]
48. Zhu, J.; Shen, Y.; Yu, X.; Guo, J.; Zhu, Y.; Zhang, Y. A facile two-step method to synthesize immobilized CdS/BiOCl film photocatalysts with enhanced photocatalytic activities. *J. Alloys Compd.* **2019**, *771*, 309–316. [[CrossRef](#)]
49. Zhang, J.; Fang, J.; Ye, X.; Guo, Z.; Liu, Y.; Song, Q.; Zheng, S.; Chen, X.; Wang, S.; Yang, S. Visible photoactivity and anti-photocorrosion performance of CdS photocatalysts by the hybridization of N-substituted carboxyl group polyaniline. *Appl. Surf. Sci.* **2019**, *480*, 557–564. [[CrossRef](#)]

50. Zhao, W.; Li, J.; She, T.; Ma, S.; Cheng, Z.; Wang, G.; Zhao, P.; Wei, W.; Xia, D.; Leung, D.Y. Study on the photocatalysis mechanism of the Z-Scheme cobalt oxide nanocubes/carbon nitride nanosheets heterojunction photocatalyst with high photocatalytic performances. *J. Hazard. Mater.* **2021**, *402*, 123839.
51. Shen, X.; Shao, H.; Liu, Y.; Zhai, Y. Synthesis and photocatalytic performance of ZnO with flower-like structure from zinc oxide ore. *J. Mater. Sci. Technol.* **2020**, *51*, 1–7. [[CrossRef](#)]
52. Zhuang, J.; Zhang, B.; Wang, Q.; Guan, S.; Li, B. Construction of novel ZnTiO₃/g-C₃N₄ heterostructures with enhanced visible light photocatalytic activity for dye wastewater treatment. *J. Mater. Sci.: Mater. Electron.* **2019**, *30*, 6322–6334. [[CrossRef](#)]
53. Venkatesh, N.; Sabarish, K.; Murugadoss, G.; Thangamuthu, R.; Sakthivel, P. Visible light-driven photocatalytic dye degradation under natural sunlight using Sn-doped CdS nanoparticles. *Environ. Sci. Pollut. Res.* **2020**, *27*, 43212–43222.
54. Abdelwahab, M.A.; El Rayes, S.M.; Kamel, M.M.; Abdelrahman, E.A. Encapsulation of NiS and ZnS in analcime nanoparticles as novel nanocomposites for the effective photocatalytic degradation of orange G and methylene blue dyes. *Int. J. Environ. Anal. Chem.* **2022**, 1–18. [[CrossRef](#)]
55. Qayoom, A.; Ashraf, I.; Rashid, A.; Ayoub, M.; Kumar, D. Synthesis and Characterization of NiS and Zn doped NiS Quantum Dots and their application in methylene blue degradation in aqueous solution. *Res Sq.* **2022**. [[CrossRef](#)]
56. Jing, C.; Zhang, Y.; Zheng, J.; Ge, S.; Lin, J.; Pan, D.; Naik, N.; Guo, Z. In-situ constructing visible light CdS/Cd-MOF photocatalyst with enhanced photodegradation of methylene blue. *Particuology* **2022**, *69*, 111–122. [[CrossRef](#)]
57. Ramasubbu, V.; Kumar, P.R.; Chellapandi, T.; Madhumitha, G.; Mothi, E.M.; Shajan, X.S. Zn (II) porphyrin sensitized (TiO₂@Cd-MOF) nanocomposite aerogel as novel photocatalyst for the effective degradation of methyl orange (MO) dye. *Opt. Mater.* **2022**, *132*, 112558. [[CrossRef](#)]
58. Alijani, H.; Abdouss, M.; Khataei, H. Efficient photocatalytic degradation of toxic dyes over BiFeO₃/CdS/rGO nanocomposite under visible light irradiation. *Diam. Relat. Mater.* **2022**, *122*, 108817.
59. Shakil, M.; Inayat, U.; Khalid, N.R.; Tanveer, M.; Gillani, S.S.A.; Tariq, N.H.; Shah, A.; Mahmood, A.; Dahshan, A. Enhanced structural, optical, and photocatalytic activities of Cd-Co doped Zn ferrites for degrading methyl orange dye under irradiation by visible light. *J. Phys. Chem. Solids* **2022**, *161*, 110419.
60. Wang, Q.; Guo, Q.; Wang, L.; Li, B. The flux growth of single-crystalline CoTiO₃ polyhedral particles and improved visible-light photocatalytic activity of heterostructured CoTiO₃/gC₃N₄ composites. *Dalton Trans.* **2016**, *45*, 17748–17758. [[CrossRef](#)] [[PubMed](#)]
61. Ma, C.M.; Yang, B.Y.; Hong, G.B. Husk of agarwood fruit-based hydrogel beads for adsorption of cationic and anionic dyes in aqueous solutions. *Molecules* **2021**, *26*, 1437. [[CrossRef](#)] [[PubMed](#)]